



## Water Vapor Exchange between Atmospheric Boundary Layer and Free Troposphere over Eastern China: Seasonal Characteristics and ENSO Anomaly

Xipeng Jin<sup>1</sup>, Xuhui Cai<sup>2\*</sup>, Xuesong Wang<sup>2</sup>, Qianqian Huang<sup>3</sup>, Yu Song<sup>2</sup>, Ling Kang<sup>2</sup>, Hongsheng Zhang<sup>4</sup>, Tong Zhu<sup>2</sup>

<sup>1</sup>Collaborative Innovation Center of Atmospheric Environment and Equipment Technology, Jiangsu Key Laboratory of Atmospheric Environment Monitoring and Pollution Control, School of Environmental Science and Engineering, Nanjing University of Information Science & Technology, Nanjing 210044, China

<sup>2</sup>State Key Lab of Environmental Simulation and Pollution Control, College of Environmental Sciences and Engineering, Peking University, Beijing 100871, China

<sup>3</sup>Institute of Urban Meteorology, Beijing 100089, China

<sup>4</sup>Department of Atmospheric and Oceanic Sciences, School of Physics, Peking University, Beijing 100871, China

*Correspondence to:* Xuhui Cai (E-mail: xhcai@pku.edu.cn)

1 **Abstract.** This study develops a quantitative climatology of water vapor exchange between the  
2 atmospheric boundary layer (ABL) and free troposphere (FT) over Eastern China. The  
3 exchange flux is estimated for January, April, July, and October over 7 years (2011 and 2014-  
4 2019) based on a water vapor budget equation using simulated meteorological data. The spatial  
5 pattern of the ABL-FT water vapor exchange flux is closely related to the topographic  
6 distribution. The seasonal variation shows that the water vapor exchange in the northern region  
7 is downward in January and October with the flux being 37%-72% of the surface evaporation  
8 to maintain the ABL moisture, while it is weak upward in April and July; the southern region  
9 presents persistently water vapor output from the ABL to the FT, with the ratio of exchange  
10 flux to surface evaporation increasing from 10% in January and October to 60%-80% in April  
11 and July. Three physical processes determine the total water vapor exchange, among which the  
12 ABL diurnal variation drives large magnitude exchange flux within the one-day cycle, but for  
13 the net monthly mean flux, the vertical motion at the ABL top is the main contributor. The  
14 anomaly of water vapor exchange in ENSO years illustrates triple antiphase distribution:  
15 strengthening in the middle area and weakening in the north and south zones of Eastern China  
16 in La Niña year, and vice versa in El Niño year. It agrees with the spatial pattern of anomalous  
17 precipitation, implying the crucial role of ABL-FT water vapor exchange in atmospheric water  
18 cycle.

19 **Keywords:** Water vapor; atmospheric boundary layer; free troposphere; vertical exchange



## 20 **1 Introduction**

21 Water vapor is a significant constituent in the atmosphere. It directly participates in  
22 fundamental physical processes, including cloud formation, precipitation, severe weather  
23 development and atmospheric circulation (Sodemann and Stohl, 2013; Wong et al., 2018;  
24 Wypych et al., 2018). Water vapor also affects important chemical reactions, such as providing  
25 OH radicals for gaseous photochemical transformations and serving as a medium in secondary  
26 aerosol formations (Pilinis et al., 1989; Tabazadeh 2000; Wu et al., 2019). Moreover, the  
27 radiation forcing of water vapor accounts for about 2/3 of the total natural greenhouse effect,  
28 which plays a vital role in climate feedback (Kiehl and Trenberth, 1997; Harries et al., 2008;  
29 Adebisi et al., 2015).

30 The distribution of water vapor in the atmospheric system depends on its source and  
31 transport processes. In general, water vapor evaporates from the Earth's surface into the  
32 atmosphere. From the meridional and zonal view, it presents a transport trend from low latitude  
33 to high latitude and from ocean to land. The horizontal transport of water vapor has been widely  
34 discussed from multiple scales. Hemispheric-scale atmospheric rivers induce large excursions  
35 of high vertically integrated water vapor from the subtropics to high latitudes (Newell et al.  
36 1992; Zhu and Newell 1998; Sodemann and Stohl, 2013). Synoptic-scale moisture flux  
37 convergence of extratropical cyclones explains the precipitations and cloud structures over the  
38 warm front and cold front (Boutle et al., 2010; Wong et al., 2018). Regional-scale transport  
39 processes are widely reported in many areas from water vapor advection and dynamical  
40 convergence (Zhou and Yu, 2005; Sun et al., 2010; Gvozdikova and Muller, 2021). However,  
41 these studies estimate vertically integrated water vapor through the atmospheric layer (usually  
42 from the surface to 300 hPa) or only focused on a certain altitude.

43 The water vapor vertical transport, especially within the troposphere, plays a key role in  
44 the atmospheric water cycle. All water vapor in the atmosphere originates from surface  
45 evaporation and is first confined in the atmospheric boundary layer (ABL, Boutle et al., 2010),  
46 which is defined as the lowest layer of the atmosphere influenced by the Earth's surface (Stull,  
47 1988). The water vapor is turbulently mixed in the ABL, making it act as a reservoir. Actually,  
48 all water vapor entering and transporting meridionally and zonally in the free troposphere (FT)  
49 is initially exported through the ABL (Bailey et al., 2013). In other words, the water vapor  
50 exchange between the ABL and the FT is a prerequisite for its large scale transport and  
51 redistribution, as well as interaction with other constituents, in the upper atmosphere. Several  
52 studies indicate the importance of this key process on precipitation (Liu et al., 2020), cloud  
53 systems (Miura et al., 2007), tropical cyclone formation (Fritz and Wang, 2013), Madden–  
54 Julian oscillation (Hirota et al., 2018), West African Monsoon Jump (Hagos and Cook, 2007),  
55 and O<sub>3</sub> vertical distributions (Andrey et al., 2014). Therefore, it is of great significance to  
56 quantify the vertical exchange of water vapor between the ABL and FT.

57 However, the exchange between the ABL and FT is not straightforward, both for water  
58 vapor or air mass. Although the diurnal variation of the ABL depth allows air constituents to



59 be entrained into and left out of this layer within its variation range, the actual exchange  
60 between ABL and FT is small on the time scale of more than one day due to the canceling  
61 effect (Hov and Flatoy, 1997; Jin et al., 2021). The current studies on water vapor vertical  
62 transport are mainly limited to complex terrain areas or special convective events. The  
63 local/mesoscale circulation induced by orographic thermal and dynamic effects is considered  
64 a key process for ABL ventilation (Kossmann et al., 1999; McKendry and Lundgren, 2000;  
65 Dacre et al., 2007). Henne et al. (2005) found that there were elevated moisture layers in the  
66 lower free troposphere in the lee of the Alps resulting from mountain venting. On average for  
67 the 12-year period, ~30% of the water vapor of the Alpine boundary layer was vented to the  
68 FT per hour during the daytime, which makes the total precipitable water within the elevated  
69 moisture layer increase by ~1.3 mm. Another simulated study indicates that the moisture  
70 exchange between the ABL and FT of mountainous topography can be about 3–4 times larger  
71 than the amount of moisture evaporated from the surface in a specific ventilation event (Weigel  
72 et al., 2007). The convective system, mainly mesoscale deep and shallow convection, is another  
73 important factor leading to the vertical transport of water vapor. The isotope observations show  
74 that the moisture transport pathways to the subtropical North Atlantic FT are linked to dry  
75 convection processes over the African continent which effectively injects humidity from the  
76 ABL to higher altitudes (Gonzalez et al., 2016; Dahinden et al., 2021). The water vapor budget  
77 of the free troposphere of the maritime tropics shows that 20% of this source comes from  
78 vertical convective transport (Sherwood, 1996). On the other hand, an idealized simulation  
79 suggests that the warm conveyor belt ascent and shallow convective processes contributed  
80 about equally to FT moisture (Boutle et al., 2010).

81 Though for these studies, general characteristics of long-term and wide-ranging ABL-FT  
82 water vapor exchange are still unknown. These characteristics are closely bound up with the  
83 atmospheric energy flow and the entire climate system, affecting clouds, precipitation and  
84 radiation (Sodemann and Stohl, 2013; Wong et al., 2018; Wypych et al., 2018). For example,  
85 small variations in upper atmospheric humidity over a large space-time scale can cause  
86 systemic changes in the hydrological cycle and atmospheric circulation (Minschwaner and  
87 Dessler, 2004; Sherwood et al., 2010; Allan, 2012). The climate state of water vapor vertical  
88 exchange flux is critical for quantifying these specific effects. To fill this knowledge gap, the  
89 present study calculates the water vapor exchange flux between the ABL and FT for 7 years  
90 (2011&2014-2019) over Eastern China (20-42°N, 108-122°E) to establish the first quantitative  
91 climatology view on this issue. The water vapor budget method is used, with the mesoscale  
92 meteorological simulation providing input data. January, April, July, and October, respectively  
93 representing winter, spring, summer, and autumn, are considered to discuss the seasonal  
94 characteristics. Interannual differences are analyzed by investigating the impact of El Niño and  
95 La Niña events. On the basis of understanding the foundational features, we further attempt to  
96 discuss the role of ABL-FT water vapor exchange playing in anomalous precipitation. The  
97 arrangement of this paper is as follows. Data and methods are described in Section 2. The  
98 seasonal characteristics and mechanism analysis, interannual variability and the relation with



99 anomalous precipitation are presented and discussed in Section 3. Finally, the findings of this  
100 study are summarized in Section 4.

## 101 **2 Data and methods**

### 102 **2.1 Observation data**

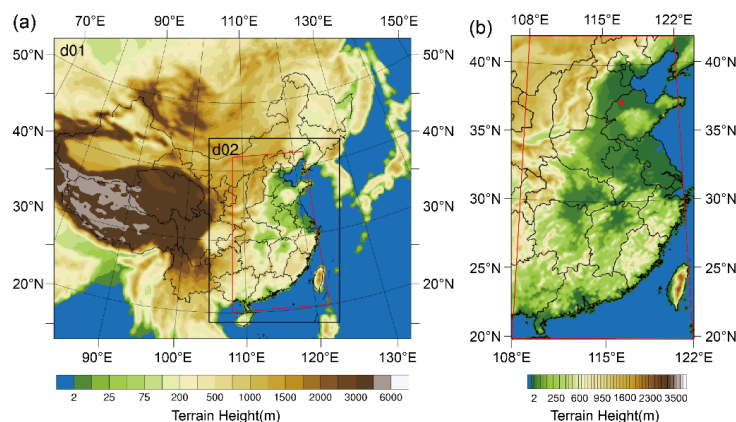
103 Intensive ABL sounding data and routine surface meteorological data were used to evaluate  
104 the performance of the Weather Research Forecast (WRF) model that provided the input data  
105 for estimating exchange flux.

106 Intensive ABL sounding data: Two field experiments of intensive GPS (Global Positioning  
107 System) sounding were carried out in Dezhou (37°16' N, 116°43' E), located in the middle of  
108 the North China Plain (NCP) (Fig. 1b), from December 25, 2017, to January 24, 2018, and  
109 from May 14 to June 14, 2018. Eight soundings were taken for each day, at 02:00, 05:00, 08:00,  
110 11:00, 14:00, 17:00, 20:00 and 23:00 LT (i.e., UTC + 8). GPS radiosonde (Beijing Changzhi  
111 Sci and Tech Co. Ltd., China) was used to obtain profiles of wind, temperature and humidity  
112 with the ascending velocity being about 3-5 m s<sup>-1</sup>. We eliminated the outliers from the original  
113 data and averaged the profiles to an effective vertical resolution of 10 m. ABL heights were  
114 determined with these data via the potential temperature profile method (Liu and Liang, 2010).  
115 The reliability of the GPS sounding data has been systematically evaluated by Li et al. (2020)  
116 and Jin et al. (2020).

117 Routine surface meteorological data: The hourly surface data of 137 routine observatories  
118 distributed within the research domain were collected from the Chinese National  
119 Meteorological Center. The dataset included information on wind speed and direction, air  
120 temperature, relative humidity, air pressure, cloud coverage and precipitation, which was used  
121 to evaluate the WRF simulation.

### 122 **2.2 Three-dimensional meteorological simulation**

123 The WRF model was conducted to provide three-dimensional meteorological data for the  
124 estimation of ABL-FT water vapor exchange flux. Two nested domains (Fig. 1a) were  
125 employed with horizontal grid resolutions of 30 and 10 km, respectively. The inner covered  
126 Eastern China (20–42°N, 108–122°E), the main research region for the ABL-FT water vapor  
127 exchange in the present work (Fig. 1b). Each domain had 37 vertical layers extending from the  
128 surface to 100 hPa, with the vertical resolution being about 20-30 m below 200 m, increasing  
129 to ~100 m at 750 m, ~250 m at 2000 m, ~350 m at 3000 m, ~600 m at 5000 m, ~900 m at 8000  
130 m, ~1300 m at 11000 m and gradually enlarging to the top of the model. There were 24 layers  
131 within 3 km to resolve the ABL and its upper FT. The meteorological initial and boundary  
132 conditions were set using the US National Center for Environmental Prediction Final Analysis  
133 (NCEP-FNL) dataset.



134

135 Figure 1. Geographical map of (a) the Weather Research and Forecast (WRF) model domains (d01 and  
 136 d02) and (b) the amplified research domain (marked with red lines). The map uses the Lambert  
 137 projection with the center meridians of 108°E in (a) and 115°E in (b). The red dot in (b) indicates the  
 138 intensive GPS sounding observatory.

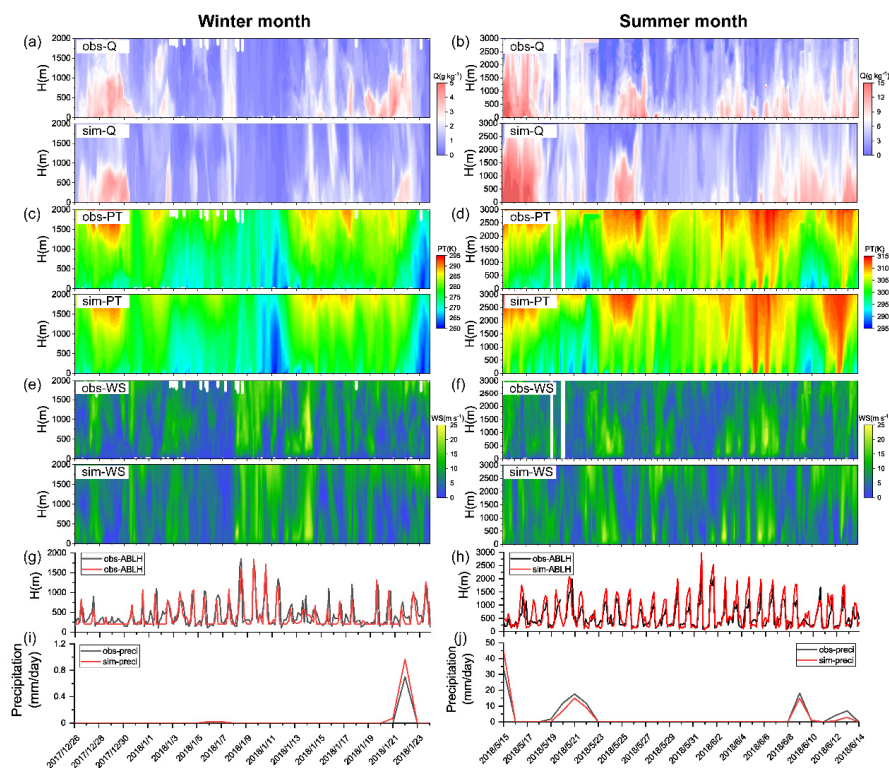
139 In order to adequately reproduce water vapor distribution and to correctly estimate the  
 140 ABL-FT exchange flux, sensitivity simulations were carried out to choose reasonable physical  
 141 parameterization schemes. We focused on the microphysical and cumulus parameterizations  
 142 that are the most relevant to the moisture simulation. Microphysics in the model includes  
 143 explicitly resolved water vapor, cloud and precipitation processes. Cumulus schemes are  
 144 responsible for the sub-grid scale effects of convection and/or shallow clouds. Vertical fluxes  
 145 due to unresolved updrafts and downdrafts are represented. Lin et al. scheme (Lin et al., 1983)  
 146 and WRF Single-Moment 6-class (WSM6) scheme (Hong and Lim, 2006) in microphysics  
 147 parameterization, and Grell-Devenyi (GD) ensemble scheme (Grell and Devenyi, 2002) and  
 148 Kain-Fritsch (KF) scheme (Kain, 2004) in cumulus parameterization were compared, which  
 149 were most commonly used in previous moisture simulation studies (Perez et al., 2010;  
 150 Gonzalez et al., 2013; Jain and Kar, 2017; Qian et al., 2020). Other physics parameterization  
 151 schemes used in this study included the Yonsei University PBL scheme (Hong et al., 2006),  
 152 Noah land surface Model (Chen and Dudhia, 2001), Dudhia shortwave radiation scheme  
 153 (Dudhia, 1989) and the rapid radiative transfer model (Mlawer et al., 1997) for longwave  
 154 radiation. WRF simulations were initialized at 00 UTC on the day and there was a 12-h spin-  
 155 up time before the start of each 48-h simulation. Domain outputs were sampled every hour for  
 156 the whole simulation period (January, April, July, and October in 2011 and 2014-2019).

157 These schemes were evaluated by comparing simulated and observed specific humidity,  
 158 temperature and wind speed, from their near-surface temporal evolution and vertical spatial  
 159 structure. Another two key parameters, ABL height and precipitation were also concerned: the  
 160 former directly affects the exchange flux results, and the latter characterizes the moisture  
 161 budget. The hourly averages of model outputs were extracted from the grid points nearest to  
 162 the observed sites for comparison. In the vertical direction, the modeled and sounding data



163 were simultaneously interpolated into the same height with 10 m intervals ranging from 50 m  
 164 to 3 km. Note that the ABL height was diagnosed with the potential temperature profile method  
 165 both for the simulations and for observation data, rather than using the default bulk Richardson  
 166 number method in the YSU scheme.

167 The results of sensitivity experiments showed that there were no appreciable differences  
 168 among various microphysical and cumulus parameterization schemes (Table S1 and S2). In  
 169 comparison, the combination of the WSM6 scheme and GD scheme performed better in  
 170 humidity simulation and was more effective in reproducing temperature, wind speed and ABL  
 171 height, especially in summer (Table S2). Therefore, these schemes were used in the present  
 172 study. Its simulation performance determines the reliability of the calculated flux results and  
 173 thus a comprehensive evaluation is provided here. The spatial-temporal evolutions of modeled  
 174 and observed meteorological fields are presented by the height-time cross sections of specific  
 175 humidity, potential temperature and wind speed, as well as the ABL height and precipitation  
 176 (Fig. 2). During the winter and summer months of the intensive GPS sounding, the simulated



177

178 Figure 2. Observed and simulated time-height cross-sections of (a-b) specific humidity, (c-d) potential  
 179 temperature, (e-f) wind speed, and temporal evolution of (g-h) ABL height and (i-j) daily cumulative  
 180 precipitation at the Dezhou site (37.27°N, 116.72°E) during winter (from December 26, 2017, to  
 181 January 24, 2018) and summer (from May 15, 2018, to June 14, 2018) months of intensive GPS  
 182 sounding field experiment. The time resolution of sounding data in (a-h) is 3-hr.



183 atmospheric thermal and dynamic structures were comparable with observations. The  
 184 alternating between dry and wet atmospheric states (Fig. 2a-b), formation and decay of upper  
 185 temperature inversion (Fig. 2c-d), and vertical location and temporal transition of the strong  
 186 and weak wind layers (Fig. 2e-f) were successfully reproduced. Accordingly, a good  
 187 correlation between the simulated and observed ABL height was achieved, both in terms of  
 188 diurnal variation and synoptic evolution lasting several days (Fig. 2g-h). The correlation  
 189 coefficients were 0.71 and 0.84 during wintertime and summertime, respectively. It should be  
 190 mentioned that there was a slight discrepancy in the modeled ABL heights (mean biases are  
 191 about 70 m and 120 m in winter and summer), which may further affect the identification of  
 192 other parameters (such as the wind component) at the ABL top and lead to uncertainty in the  
 193 calculation results. This impact will be quantitatively analyzed in the discussion section.  
 194 Another concerned meteorological factor, the daily cumulative precipitation was also evaluated,  
 195 which showed a consistent evolution in observation and simulation (Fig. 2i-j) with correlation  
 196 coefficients as high as 0.99 and 0.91 ( $p < 0.05$ ) in winter and summer respectively,  
 197 demonstrating that the moisture budget is accurately captured by the WRF simulations. Overall,  
 198 the model showed the ability to capture the major variation of observed atmospheric thermal-  
 199 dynamical structures reasonably, which ensures the validity of the meteorological inputs for  
 200 the ABL-FT exchange flux calculation.

### 201 2.3 ABL-FT water vapor exchange flux

202 Similar to mass vertical exchange (Sinclair et al. 2010; Jin et al., 2021), the estimation of  
 203 ABL-FT water vapor exchange flux in this study was based on an ABL water vapor budget  
 204 equation established by Boutle et al. (2010):

$$\begin{aligned}
 205 \quad \frac{\partial}{\partial t} \left( \int_0^h \rho q dz \right) = & - \left( \frac{\partial}{\partial x} \int_0^h \rho q u dz + \frac{\partial}{\partial y} \int_0^h \rho q v dz \right) + (\rho q)_h \left( \frac{\partial h}{\partial t} \right) \\
 206 \quad & - (\rho q)_h (\vec{U} \cdot \vec{n})_h - (\rho \overline{w'q'})_h + (\rho \overline{w'q'})_0 + P, \quad (1)
 \end{aligned}$$

207 where  $\rho$  is air density,  $q$  is water vapor mixing ratio,  $h$  is the ABL height,  $\vec{U} = (u, v, w)$  is  
 208 wind vector,  $\vec{n} = \left( -\frac{\partial h}{\partial x}, -\frac{\partial h}{\partial y}, 1 \right)$  is the unit normal vector perpendicular to the ABL top  
 209 surface,  $w'$  and  $q'$  are the fluctuation values of vertical velocity and water vapor content  
 210 respectively.  $P$  is the precipitation. Subscripts  $h$  and  $0$  indicate quantities at the ABL top and  
 211 the surface. The first term on the right side of Eq. (1) represents horizontal  
 212 convergence/divergence within the ABL, the second term indicates the local change in ABL  
 213 depth, the third term indicates vertical advection across the ABL top, the fourth and fifth terms  
 214 are turbulent transport at the ABL top and the surface respectively, and the last term indicates  
 215 the net precipitation falling through the ABL.

216 Denoting the water vapor vertical exchange flux between the ABL and FT as  $F$  (positive  
 217 values represent upward transport), it can be further written as:

$$218 \quad F = -((\rho q)_h \left( \frac{\partial h}{\partial t} \right) - (\rho q)_h (\vec{U} \cdot \vec{n})_h - (\rho \overline{w'q'})_h)$$



$$\approx -(\rho q)_h \frac{\partial h}{\partial t} + (\rho q)_h \left( u_h \frac{\partial h}{\partial x} + v_h \frac{\partial h}{\partial y} \right) - (\rho q)_h w_h. \quad (2)$$

219 Since turbulent transport between the ABL and FT is typically related with dryer air that does  
220 not affect the total moisture content,  $(\overline{w'q'})_h$  is usually considered to be a negligible  
221 contribution to the ABL-FT water vapor exchange flux (Boutle et al., 2010). Specifically, the  
222 finite difference method was adopted for calculation with the time step being 1 hr, and the  
223 horizontal dimensions of the model grid being 10 km. The ABL heights were obtained from  
224 the hourly output of the WRF model. Other variables were extracted from the vertical level  
225 closest to the top of the ABL. It is clear that the water vapor vertical exchange flux between  
226 the ABL and FT is determined by i) the local temporal variation of ABL height,  $\frac{\partial h}{\partial t}$ , allowing  
227 the water vapor entrained into the ABL or left in the upper atmosphere; ii) the spatial variation  
228 of the ABL, making water vapor horizontally advected across an inclined ABL top; and iii) the  
229 vertical advection motion, carrying water vapor downward/upward through the interface  
230 between the ABL and FT. These three flux components are denoted as  $F_{local}$ ,  $F_{hadv}$ , and  $F_{vadv}$ ,  
231 and their contributions and evolutions will be discussed in the following.  
232

### 233 3 Results and discussion

234 The present study is based on a 7-year flux calculation. The years 2011&2014-2019 are  
235 selected for analysis, which includes typical La Niña, El Niño, and neutral years (Marchukova  
236 et al., 2020; You et al., 2021; Felix Correia Filho et al., 2021), and are considered to be valid  
237 and concise datasets to reflect the characteristics of water vapor exchange between the ABL  
238 and FT. Their climatic representativeness is demonstrated using a long-term historical dataset  
239 provided by the fifth generation ECMWF (European Centre for Medium Range Weather  
240 Forecasts) reanalysis. We compare the features of key meteorological elements during the  
241 study period (2011&2014-2019) and over the past 30 years (1990-2019) by the Kolmogorov-  
242 Smirnov test (K-S test) and histogram analysis. Temperature, three-dimension wind component,  
243 specific humidity both near the surface and at the upper-level, as well as the ABL height and  
244 precipitation are concerned. The K-S test indicates that there is no significant difference (with  
245 a confidence level of 95%) between the 7-year sample period and the 30-year historical dataset  
246 for these variables (Table S3). The histogram analysis further illustrates that their normalized  
247 frequencies in the research samples are similar to that in the long-term historical data (Fig. S1).  
248 Also, the annual variation of the two sets of data presents a high consistency, with similar mean  
249 values and standard deviations (Fig. S2). The above analysis verifies that the 7-year samples  
250 adopted in this study can represent the long-term climatology, and be promising to obtain  
251 climatic features of water vapor exchange between the ABL and FT. The basic temporal and  
252 spatial patterns, influencing mechanism, and relationship with ENSO and extreme precipitation  
253 are revealed as follows.

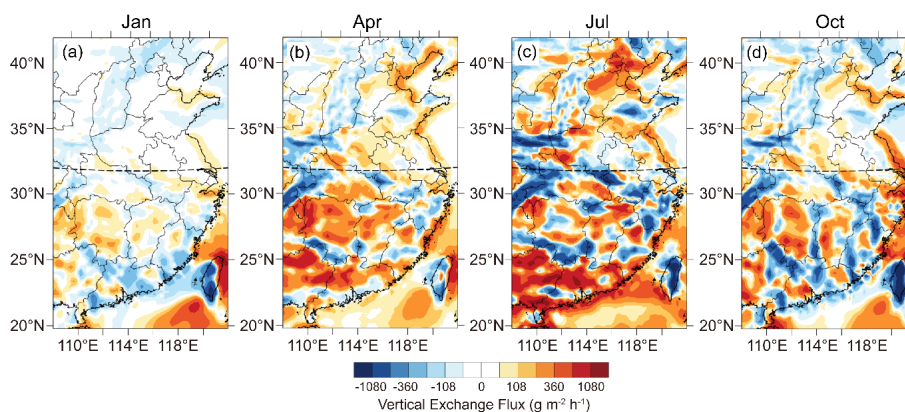




254 **3.1 Seasonal generality and variability**

255 **3.1.1 Spatial distribution**

256 Figure 3 shows the spatial distribution of water vapor exchange flux between the ABL and  
257 FT in the research domain (20-42°N, 108-122°E, marked by red lines in Fig.1), averaged over  
258 all 7-year (2011, 2014-2019) for January, April, July, and October. It is obvious that the ABL-  
259 FT water vapor exchange in the north and south of the research domain is different, because  
260 they are affected by subtropical and temperate climates, respectively (Domroes and Peng, 1988;  
261 Zheng et al. 2013; Zhang et al., 2020). Therefore, the southern (20-32°N, 108-122°E) and  
262 northern (32-42°N, 108-122°E) regions are divided for analysis (the boundary marked in Fig.  
263 3). Water vapor exchange is more active in the southern region with more pronounced spatial  
264 variability, and tends to output from the ABL. In the northern region, vertical exchange fluxes  
265 and spatial differences are relatively small. From another perspective, the vertical exchange of  
266 water vapor is closely related to the topographic distribution (Fig. 1b), which is manifested as  
267 strong exchange activities usually occurring around mountainous or coastal areas, both in the  
268 northern and southern regions. This feature is similar to the spatial pattern of the air mass  
269 exchange flux between the ABL and the FT indicated by Jin et al. (2021). It is the result of the  
270 dynamical interaction of topography on the synoptic system, and thermal property difference  
271 over the heterogeneous underlying surface (Kossmann et al., 1999; Dacre et al., 2007; Jin et  
272 al., 2021). These phenomena will be detailedly explained in the mechanism analysis in Sect.  
273 3b.



274

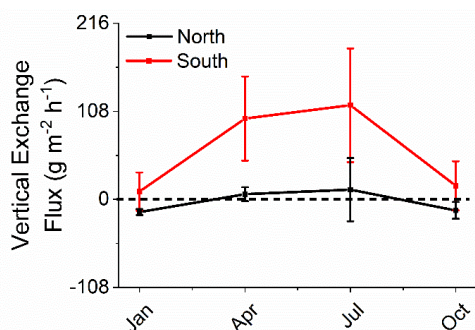
275 Figure 3. Spatial distribution of ABL-FT water vapor exchange fluxes in Eastern China, averaged over  
276 7-year for (a) January, (b) April, (c) July, and (d) October. Black dashed lines mark the boundary  
277 between the northern (32-42°N, 108-122°E) and southern (20-32°N, 108-122°E) regions. Positive and  
278 negative fluxes (warm and cool colors) represent water vapor upward and downward transport at the  
279 ABL and FT interface.



### 280 3.1.2 Seasonal difference

281 Corresponding to Fig. 3, the spatial means of ABL-FT water vapor exchange flux and their  
282 seasonal evolutions for northern and southern regions are shown in Fig. 4. They are obtained  
283 by grid averaging in the ranges of 32-42°N, 108-122°E and 20-32°N, 108-122°E, respectively.  
284 Obviously, the exchange flux varies from season to season in both regions. For the northern  
285 region, winter and autumn (represented by January and October, respectively) are characterized  
286 by water vapor transport downward from the FT into the ABL, with the spatial mean fluxes of  
287  $-15.6$  and  $-18.8 \text{ g m}^{-2} \text{ h}^{-1}$  ( $1 \text{ g m}^{-2} \text{ h}^{-1} = 10^{-3} \text{ mm h}^{-1}$ ) and the standard deviation of  $3.6$  and  $8.6$   
288  $\text{g m}^{-2} \text{ h}^{-1}$  over 7 years. While in spring and summer (represented by April and July, respectively),  
289 the northern region as a whole presents an upward export of water vapor from the ABL to the  
290 FT, with the regional mean fluxes being  $6.4$  and  $11.9 \text{ g m}^{-2} \text{ h}^{-1}$ . They are characterized by more  
291 significant inter-annual variations than the exchange fluxes in the cold seasons. In the southern  
292 region, the water vapor vertical exchange is featured with ABL output in all seasons, with a  
293 winter minimum and a summer maximum. The mean upward fluxes vary greatly, showing one  
294 order of magnitude greater in April and July ( $99.1$  and  $115.51 \text{ g m}^{-2} \text{ h}^{-1}$ ) than in January and  
295 October ( $9.6$  and  $16.7 \text{ g m}^{-2} \text{ h}^{-1}$ ), accompanied by the larger standard deviation ( $50.4$  and  $68.4$   
296  $\text{g m}^{-2} \text{ h}^{-1}$ ). The notable interannual variability in the warm season may be related to the ENSO  
297 phenomenon, which will be discussed in the following section.

298 In order to better understand the magnitude of water vapor exchange between the ABL and  
299 FT, we compare the transport flux with the surface evaporation rate (Table 1). It indicates the  
300 “emission intensity” of water vapor from the surface, which varies in different regions and  
301 seasons. The surface evaporation rates in the northern and southern regions have maximums in  
302 summer ( $122.4 \text{ g m}^{-2} \text{ h}^{-1}$  and  $194.4 \text{ g m}^{-2} \text{ h}^{-1}$ ) and minimums in winter ( $21.6 \text{ g m}^{-2} \text{ h}^{-1}$  and  $108.0$   
303  $\text{g m}^{-2} \text{ h}^{-1}$ ). Obviously, the evaporation in the north is weaker than that in the south, especially  
304 in winter, it is only one-fifth of that in summer. Consequently, for the northern region, during  
305 the cold seasons with the dry land surface, the ABL-FT water vapor exchange is downward  
306 and the input flux is 37%-72% of the surface evaporation rate. Although the specific humidity  
307 decreases with height, counter-gradient transport still occurs reasonably because the ABL-FT  
308 exchange is a typically non-local mixing process (Stull 1988; van Dop and Verver, 2001;  
309 Ghannam et al., 2017). This suggests the ABL is a net moisture sink of upper layer FT air,  
310 which plays a role in maintaining water vapor within this layer. As surface evaporation  
311 intensifies in the warm months, water vapor is exported from the ABL in April and July, and  
312 the upward flux accounts for 10% of the evaporation rate. In the southern region with relatively  
313 strong evaporation, the ABL water vapor is always transported upward to the FT. The output  
314 flux is about 10% of the evaporation rate in January and October, and this ratio is as high as  
315 60%-80% in April and July, indicating that the ABL acts as an effective water vapor source to  
316 the upper atmosphere.



317

318 Figure 4. Seasonal variation of average ABL-FT water vapor exchange fluxes and their standard  
 319 deviations over the northern region (32-42°N, 108-122°E) and southern region (20-32°N, 108-122°E)  
 320 during 7 years. Positive and negative fluxes represent water vapor upward and downward transport  
 321 between the ABL and FT.

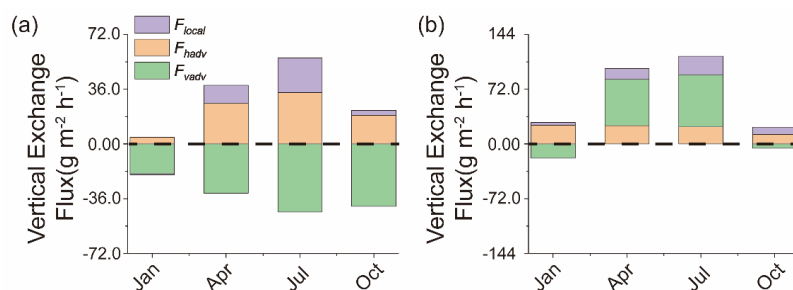
322 Table1. Comparison of ABL-FT water vapor exchange flux ( $\text{g m}^{-2} \text{h}^{-1}$ , positive for upward, negative for  
 323 downward) and surface evaporation rate ( $\text{g m}^{-2} \text{h}^{-1}$ , positive for upward) in the northern and southern  
 324 regions.

Region	Process	Jan	Apr	Jul	Oct
North	ABL-FT exchange	-15.6	6.4	11.9	-18.8
	Surface evaporation	21.6	61.2	122.4	50.4
South	ABL-FT exchange	9.6	99.1	115.5	16.7
	Surface evaporation	108.0	115.2	194.4	144.0

### 325 3.2 Main influential mechanism

326 As shown in Eq. (2), three physical terms contribute to the total ABL-FT exchange, i.e., the  
 327 local temporal variation of ABL height ( $F_{local}$ ), the horizontal advection across the spatial  
 328 inclined ABL top ( $F_{hadv}$ ), and the vertical motion through the ABL-FT interface ( $F_{vadv}$ ). It is  
 329 of interest to clarify the specific effects of these factors on water vapor vertical exchange and  
 330 their seasonal characteristics. Results of the monthly mean and diurnal cycle over the 7 years  
 331 are presented below respectively.

332 The monthly mean results show that the term  $F_{vadv}$  is the most significant to total ABL-FT  
 333 moisture exchange flux (Fig. 5, green bar). In the northern region, this term produces persistent  
 334 downward flux ( $-19.5 \sim -44.7 \text{ g m}^{-2} \text{h}^{-1}$ , Fig. 5a), which substantially offsets the upward flux  
 335 caused by the other two terms, so that the ABL water vapor presents net input during cold  
 336 months (i.e., January and October) and weak output in warm seasons (i.e., April and July). For  
 337 the southern region, it induces small downward fluxes in January and October ( $-18.6$  and  $-5.5$   
 338  $\text{g m}^{-2} \text{h}^{-1}$ ) while large upward flux in April and July ( $60.7$  and  $68.6 \text{ g m}^{-2} \text{h}^{-1}$ ), which results in  
 339 the total water vapor exchange as weak and strong output from the ABL during cold and warm  
 340 months, respectively (Fig. 5b).



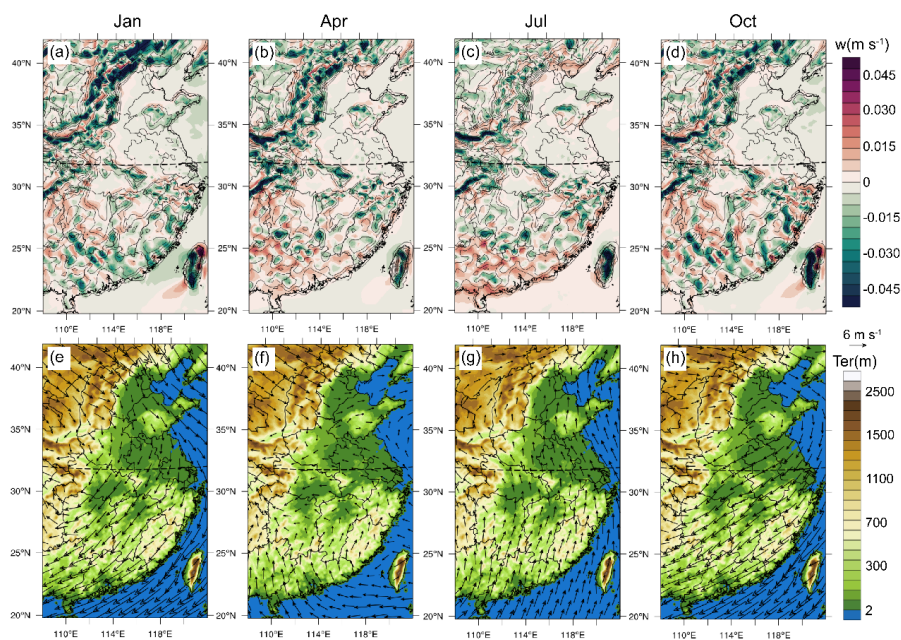
341

342 Figure 5. Contributions of three components ( $F_{local}$ ,  $F_{hadv}$ , and  $F_{vadv}$ ) to the total ABL-FT water vapor  
 343 exchange flux. Results are spatial mean over the (a) northern (32-42°N, 108-122°E) and (b) southern  
 344 (20-32°N, 108-122°E) regions of Eastern China respectively.  $F_{local}$ : local temporal variation of ABL  
 345 height (purple bar);  $F_{hadv}$ : advection across the spatial inclined ABL top (yellow bar);  $F_{vadv}$ : vertical  
 346 motion through the ABL-FT interface (green bar). Positive and negative fluxes represent water vapor  
 347 upward and downward transport between the ABL and FT.

348 The upward/downward transport of water vapor caused by the term  $F_{vadv}$  depends on the  
 349 direction of the vertical motion. The spatial distributions of the vertical velocity are presented  
 350 in Fig. 6, accompanied by horizontal wind fields at the ABL top, as well as terrain heights. The  
 351 upward motions usually occur on the windward of the mountains, while the descending  
 352 velocities appear on the leeward side, in each season. This is attributed to the dynamic forcing  
 353 of the terrain on seasonal mean winds. Due to the alternation of winter and summer monsoons  
 354 throughout the year, the vertical motion pattern varies accordingly in four representative  
 355 months (Fig. 6a-d). In the winter, the Siberian high invades from the northwest and forms  
 356 strong northerly winds (Fig. 6e). In the northern region, the prevailing northwest airflows  
 357 overcome the obstruction of Taihang Mountain and intensely descend on its leeward side (Fig.  
 358 6a). As the air migrates south, the dominant airflow deflects northeasterly (Fig. 6e), and the  
 359 vertical motion manifests more upward velocities in front of the major mountainous region,  
 360 and more downward velocities behind these mountains (Fig. 6a). During the summer, southerly  
 361 air flows dominate eastern China and gradually weaken from south to north (Fig. 6g). The  
 362 southern region is characterized by obvious forced uplift on the windward side of the major  
 363 mountains (Fig. 6c). The onshore airflow convergence of the prevailing southerly winds in  
 364 coastal areas also produces upward motions (Fig. 6c). These factors are conducive to the  
 365 vertical output of ABL water vapor in the southern region during warm months. The northern  
 366 region is less invaded by the summer monsoon: only the eastern part of the NCP is affected by  
 367 southerly winds to induce upward motion in the piedmont, while the western part is still  
 368 dominated by westerly winds leading to systematic subsidence (Fig. 6c, g). The general  
 369 patterns of vertical velocity fields provide an explanation for the water vapor exchange fluxes  
 370 caused by the term  $F_{vadv}$ . It is noticed that, although the ABL-FT water vapor exchange fluxes  
 371 in Fig. 3 are averages over 7 years, there still exists obvious spatial heterogeneity. Smooth  
 372 variations in both the mean wind field (Fig. 6e-h) and mean ABL height (Fig.S5) indicate these  
 373 two factors are not related to the flux heterogeneity. But there indeed exists discontinuous



374 structures in the vertical velocity fields at the ABL top (Fig.6a-d), which is significant to water  
 375 vapor exchange flux. There can be smaller-scale secondary vertical motion being stimulated  
 376 when prevailing airflows encounter diverse terrains (Fig. S4). Multiscale dynamical  
 377 interactions between complex terrain and synoptic processes should be of great significance to  
 378 the water vapor exchange between the ABL and FT.



379

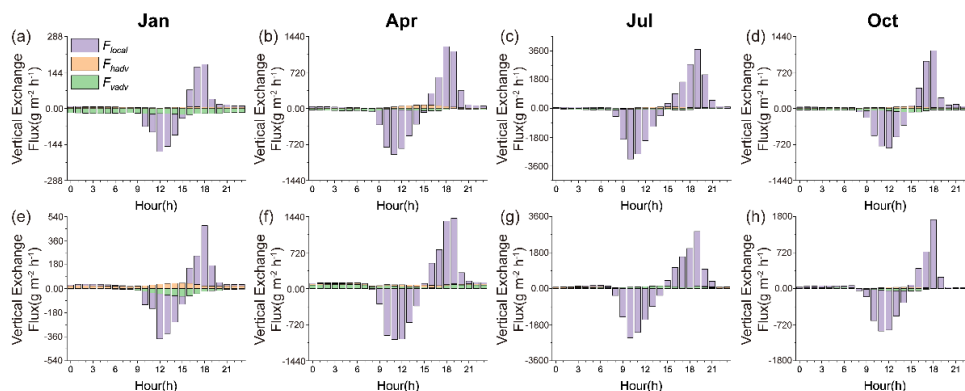
380 Figure 6. Spatial distribution of (a-d) vertical velocities at the ABL top and (e-h) terrain height  
 381 superposed with horizontal wind vectors averaged over 7-year for January, April, July, and October.  
 382 Positive values represent upward motions and the contours in (a-d) represent the terrain height. Black  
 383 dashed lines mark the boundary between the northern (32-42°N, 108-122°E) and southern (20-32°N,  
 384 108-122°E) regions.

385 The horizontal advection term  $F_{hadv}$  tends to allow water vapor to be out of the ABL and  
 386 the magnitude increases in spring and summer (Fig. 5, yellow bar). This water vapor exchange  
 387 component mainly occurs in the mountain-plain transition zone and the land-ocean boundary  
 388 (Fig. S3e-h), where the ABL is unevenly distributed due to the heterogeneous surface  
 389 properties (Fig. S5). During the warm season, the thermal difference is more obvious with the  
 390 solar radiation strengthening and thereby with larger spatial variation of the ABL, especially  
 391 in the northern region. This explains the seasonal variation of the water vapor exchange flux  
 392 caused by the term  $F_{hadv}$ .

393 The temporal ABL height variation term  $F_{local}$  contributes relatively less to the total water  
 394 vapor exchange (Fig. 5, purple bar). Noticeably, this average flux component is positive, being  
 395 negligible in autumn and winter ( $0.7\sim 3.3 \text{ g m}^{-2} \text{ h}^{-1}$ ), but becoming relatively pronounced in  
 396 spring and summer ( $12.0\sim 24.5 \text{ g m}^{-2} \text{ h}^{-1}$ ). This is inconsistent with the air mass exchange



397 between the ABL and FT, in which the monthly average flux caused by this term is always  
 398 insignificant because the ABL entrainment and detrainment of the air mass cancel out each  
 399 other in a diurnal cycle (Jin et al., 2021). To understand more details of the term  $F_{local}$  in the  
 400 ABL-FT water vapor exchange, the mean diurnal variation of the exchange flux is derived and  
 401 shown in Fig. 7.



402

403 Figure 7. Diurnal variation of the three exchange flux components ( $F_{local}$ ,  $F_{hadv}$ , and  $F_{vadv}$ ) over the  
 404 (a-d) northern region (32-42°N, 108-122°E) and (e-f) southern region (20-32°N, 108-122°E) averaged  
 405 for (a, e) January, (b, f) April, (c, g) July, and (d, h) October.  $F_{local}$ : local temporal variation of ABL  
 406 height (purple bar);  $F_{hadv}$ : advection across the spatial inclined ABL top (yellow bar);  $F_{vadv}$ : vertical  
 407 motion through the ABL-FT interface (green bar). Positive and negative fluxes represent water vapor  
 408 upward and downward transport between the ABL and FT.

409 At a first sight of the daily cycle,  $F_{local}$  is the absolutely dominant term in all seasons and  
 410 both northern and southern regions (Fig. 7, purple bar), corresponding to the diurnal variation  
 411 of the ABL height (shown in Fig. S6). When the unstable ABL develops in the morning, the  
 412 water vapor in the residual layer is entrained into the ABL; while as the daytime ABL collapses  
 413 in the later afternoon, a large part of water vapor is left aloft the newly formed stable ABL.  
 414 Note that, unlike the air mass exchange at the ABL top, the water vapor entrained (input) flux  
 415 is less than the output flux, especially in spring and summer. This difference can be attributed  
 416 to the fact that the surface is, in general, a continuous evaporation source throughout a diurnal  
 417 cycle. Turbulent mixing brings water vapor upward in the ABL depth, and forms a net upward  
 418 flux across the ABL top. This is also the reason why a larger magnitude of  $F_{local}$  exists in the  
 419 warm seasons when there is more strong surface evaporation. Although the ABL temporal  
 420 variation term  $F_{local}$  dominates the diurnal variation of the total ABL-FT moisture exchange  
 421 flux, it contributes only a weak net output of water vapor in a monthly average flux, in  
 422 comparison with the vertical motion term  $F_{vadv}$ , as mentioned above.

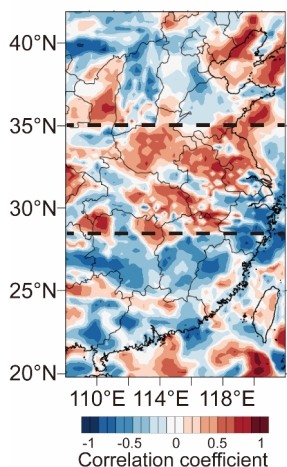
### 423 3.3 Interannual variability and its relation with anomalous precipitation

424 A climatic mean of the ABL-FT water vapor exchange over eastern China is presented  
 425 above. Critically linked to the atmospheric water cycle, the exchange flux and its interannual



426 variation are of great interest. It is well known that the atmospheric water cycle is significantly  
427 affected by El Niño and southern oscillation (ENSO), which is a joint phenomenon of the ocean  
428 and the atmosphere appearing as a recurring anomaly of the sea surface temperatures in the  
429 tropical Pacific and a seesaw of sea level pressure anomalies between Tahiti and Darwin. The  
430 El Niño (warm phase) and La Niña (cold phase) are the two extremes of ENSO (Walker and  
431 Bliss, 1932, 1937; Kousky et al., 1984; Wolter and Timlin, 2011). Considerable work has been  
432 conducted on the relationship between ENSO and wet and dry variability, water vapor  
433 horizontal transport, and precipitation events (Diaz, 2000; Knippertz and Wernli, 2010; Felix  
434 Correia Filho et al., 2021). However, little is known about the ABL-FT water vapor exchange  
435 during ENSO events. Here we take July as the research object, the month with the largest  
436 variability (shown in Fig. 4), to investigate the interannual difference of ABL-FT water vapor  
437 exchange fluxes affected by the ENSO phenomenon.

438 The correlation between the water vapor exchange flux anomalies and the Niño-3.4 index  
439 during the study period (2011&2014-2019) is quantitatively calculated. The former (anomaly  
440 or variability) is derived from the difference of each year with the 7-year average, and the latter  
441 is obtained from the website of [https://psl.noaa.gov/gcos\\_wgsp/Timeseries/Nino34/](https://psl.noaa.gov/gcos_wgsp/Timeseries/Nino34/),  
442 representing the average equatorial sea surface temperature across the Pacific from about the  
443 dateline to the South American coast (5°N-5°S, 170°W-120°W), which is the most commonly  
444 used indices to define El Niño and La Niña event. The statistical result shows that there is a  
445 significant correlation between the two factors (with a confidence level of 95%). A negative-  
446 positive-negative triple distribution is presented in the correlation map (Fig. 8). On this basis,  
447 the sensitive areas are identified, in which the water vapor exchange fluxes are further analyzed.  
448 For the central region (28-35°N, 108-122°E) with obvious positive correlation, the mean  
449 vertical output flux of water vapor is enhanced by about 57.6~151.2 g m<sup>-2</sup> h<sup>-1</sup> in La Niña years

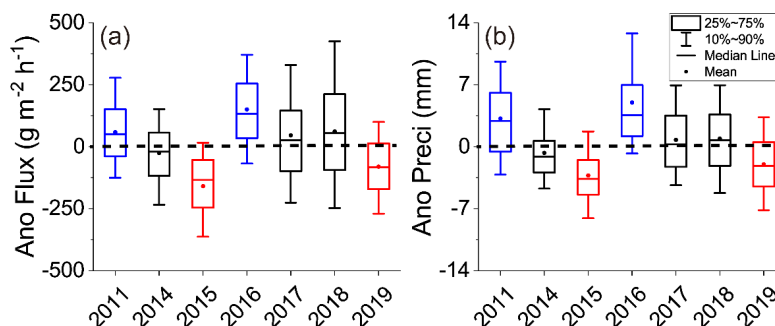


450

451 Figure 8. Spatial distribution of correlation coefficient between the water vapor exchange flux  
452 anomalies and Niño-3.4 index in July for 7 years. The black dashed lines indicate the tripole distribution.



453 (2011 and 2016, blue boxes in Fig. 9a), and vice versa in El Niño years (2015 and 2019, red  
 454 boxes in Fig. 9a), and the flux anomalies are close to 0 in neutral years (2014, 2017, and 2018,  
 455 black boxes in Fig. 9a). In south and north areas with negative correlation coefficients, it is  
 456 reversed. That is, the ABL moisture ventilation flux weakens  $79.2\sim 140.4\text{ g m}^{-2}\text{ h}^{-1}$  in La Niña  
 457 years and increases  $108\sim 194\text{ g m}^{-2}\text{ h}^{-1}$  in El Niño years (figure not shown). This provides an  
 458 explanation for the interannual variation of the water vapor exchange flux mentioned in Sect.  
 459 3a. Further analysis of the three physical processes causing vertical transport suggests that the  
 460 ENSO phenomenon affects the water vapor exchange mainly by modifying the vertical motion  
 461 patterns at the ABL top, which may fundamentally change other weather processes in this  
 462 region, e.g., the distribution of precipitation.



463

464 Figure 9. Anomalies of (a) water vapor exchange flux and (b) precipitation in July over the central  
 465 region ( $28\text{-}35^{\circ}\text{N}$ ,  $108\text{-}122^{\circ}\text{E}$ , indicated in Fig. 8) during 2011&2014-2019. Blue, red and black indicate  
 466 La Niña years, El Niño years and neutral years, respectively. Upper and lower sides of the box are the  
 467 75th and 25th percentile, and whiskers are the 90th and 10th percentile. Hollow squares and black lines  
 468 in the box are mean and median.

469 Previous observation climatological studies have indicated that the summer precipitation  
 470 anomalies in La Niña/ El Niño years are characterized by a tripolar distribution over eastern  
 471 China (Wang et al., 2020), similar to water vapor exchange flux anomalies revealed in this  
 472 work. It is of interest to investigate the relationship between water vapor vertical exchange and  
 473 precipitation under the influence of ENSO. Taking the central region ( $28\text{-}35^{\circ}\text{N}$ ,  $108\text{-}122^{\circ}\text{E}$ ) as  
 474 an example, the precipitation anomalies present a good correspondence with the variations of  
 475 the ABL-FT water vapor exchange flux (Fig. 9). Specifically, precipitation increases (decreases)  
 476 about  $3.2\text{-}6.9\text{ mm}$  ( $2.8\text{-}3.5\text{ mm}$ ) when the vertical output of water vapor intensifies (weakens)  
 477 in La Niña (El Niño) years. That is, enhanced water vapor output flux from the ABL to the FT  
 478 tends to produce increased precipitation and vice versa. These results imply that, upper layer  
 479 FT water vapor supplement from the ABL can also be a significant factor to change regional  
 480 precipitation, in addition to horizontal transport.

481 It should be stated that the above results are preliminary and rough, due to the limitations  
 482 of the sample. The response of the ABL-FT water vapor exchange to ENSO, and its impact on  
 483 precipitation, are complicated. The isolated patches in Fig. 8, as well as the box and whisker in





484 Fig. 9 (being 75th-25th and 90th-10th percentile of the flux/precipitation anomalies), reflect  
485 the complex spatial variability over the research domain, which is not thoroughly analyzed in  
486 the current work. Nevertheless, this general result points to an association among ABL-FT  
487 water vapor exchange, ENSO, and extreme precipitation, which should be paid more attention  
488 to in future research.

### 489 3.4 Discussion

490 The present results are based on numerical simulations. Although reasonable  
491 parameterization schemes are chosen according to sensitivity experiments, and the model  
492 performance is also evaluated by observational data, there are inevitable uncertainties in the  
493 modeled meteorological fields, which may directly affect the estimate of ABL-FT water vapor  
494 exchange flux. For example, the difference between the simulated ABL height and the observed  
495 value (~70 m and 120 m in winter and summer) brings ~30% uncertainty to the acquisition of  
496 vertical velocity at this level, which may affect the accuracy of the flux results in a similar  
497 magnitude. In addition, ignoring the turbulence term in this study may also reduce the accuracy  
498 of the results. Nevertheless, this work presents a general view of long-term and large-scale  
499 ABL-FT water vapor exchange over Eastern China.

500 The water vapor exchange in the climatological sense presents a significant regional  
501 division of north and south China, due to their quite distinct climatic features. In addition to  
502 this general pattern, the spatial heterogeneity associated with the topographic distribution is  
503 also noteworthy. We try to sort out the vertical exchange fluxes of water vapor over the ocean,  
504 plain and mountain, roughly by the altitude below 0m, between 0-200m and greater than 200m.  
505 The statistical results show that the ocean and plain are characterized by the upward output of  
506 water vapor from the ABL, while the transport is downward over the mountainous region. To  
507 further discuss the causes of these results is of interest, but it is quite beyond our objectives in  
508 this preliminary work. The present results indicate the importance of interaction between  
509 synoptic airflow and complex terrain in the long run. It suggests that topographic ventilation is  
510 not only caused by mesoscale circulations such as daytime upslope winds/sea breezes around  
511 mountains/coasts (Henne et al., 2004; Weigel et al., 2007) or convective activities on a  
512 relatively small scale or a specific time (Gonzalez et al., 2016; Dahinden et al., 2021).  
513 Dynamical forcing of terrain on seasonal airflow or synoptic winds is more essential, which  
514 induces vertical motion and leads to systematic water vapor exchange.

515 Moreover, the climatology of water vapor exchange flux between ABL and FT provides a  
516 quantitative background for investigating weather processes, radiation feedback and climate  
517 changes. Water vapor entering the FT may provide more latent heat to the energy flows and  
518 further affect synoptic systems. It is also involved in the radiative budget to influence climate.  
519 Previous model simulations and observations indicate that small yet systematic changes in the  
520 humidity of upper atmosphere modulate the magnitude of the hydrological cycle and radiative  
521 feedback, including clouds and precipitation (Minschwaner and Dessler, 2004; Sherwood et al.,  
522 2010; Allan, 2012). Our results also demonstrate a notable relation between precipitation



523 anomalies and ABL-FT water vapor exchange patterns. Based on the quantitative results in this  
524 study, the specific role of ABL - FT water vapor exchange in Earth's energy flows and climate  
525 system might be studied further in the future.

#### 526 **4 Summary**

527 In this study, we developed a climatology of water vapor exchange flux between the ABL  
528 and FT, based on 7-year meteorological modeling data. The ABL water vapor conservation  
529 method was used to estimate the vertical exchange flux across the ABL-FT interface. Spatial  
530 distribution and seasonal characteristics of the water vapor exchange were presented, and the  
531 interannual variability was simply discussed through their variations in ENSO events. Three  
532 influential mechanisms of the water vapor exchange between ABL and FT were also analyzed.  
533 The major findings of this work are the following:

534 The spatial pattern of the ABL-FT water vapor exchange flux was closely related to the  
535 topographic distribution in each seasonal representative month (January, April, July and  
536 October), with strong exchange activities occurring over mountainous areas and coastal areas.  
537 In the northern region (32-42°N, 108-122°E), the winter and autumn months (January and  
538 October) were characterized by the net downward flux of water vapor ( $-15.6$  and  $-18.8$  g m<sup>-2</sup>  
539 h<sup>-1</sup>), being 37%-72% of the surface evaporation. The water vapor downward transport from  
540 FT was another source for ABL moisture maintenance in these drier and colder seasons. During  
541 the spring and summer months (April and July), the water vapor was exported from the ABL  
542 with the regional average flux of 6.4 and 11.9 g m<sup>-2</sup> h<sup>-1</sup>. In the southern region (32-42°N, 108-  
543 122°E), the water vapor vertical exchange at the ABL top was persistently upward to the FT.  
544 And the flux accounted for about 10% of the surface evaporation rate in autumn and winter  
545 (9.6 and 16.7 g m<sup>-2</sup> h<sup>-1</sup>), and increased to 60%~80% during warm seasons of spring and summer  
546 (115.5 and 99.1 g m<sup>-2</sup> h<sup>-1</sup>). Clearly, the ABL acted as a channel to transport surface moisture to  
547 the FT, particularly in the southern region during summer.

548 Three physical terms determined the total ABL-FT exchange of water vapor, i.e., the  
549 diurnal variation of ABL height, the air advection across the inclined ABL top, and the vertical  
550 motion through the ABL-FT interface. The respective contributions of these three terms were  
551 revealed. The first term showed prevailing diurnal variation, but achieved only a small upward  
552 water vapor transport in the average of longer than a one-day cycle. The second term tended to  
553 cause the water vapor output from the ABL, especially in spring and summer. In a view of the  
554 monthly average, the third term was the most prominent, which played a determinative role in  
555 contributing total downward flux in the northern cold months and the total upward flux in the  
556 southern warm months.

557 Interannual variability of ABL-FT water vapor exchange was demonstrated by the results  
558 in ENSO event years. The exchange flux was strengthened in the middle zone and weakened  
559 in the north and south of Eastern China in La Niña year (vice versa in El Niño year), presenting  
560 as a triple anti-phase distribution. Moreover, the exchange flux variation illustrated good



561 correspondence with precipitation anomalies, shown as precipitation increasing accompanied  
562 by stronger water vapor output in the middle area and precipitation decreasing in north and  
563 south of Eastern China with the less upward flux of moisture in La Niña years, while the El  
564 Niño years are opposite. This phenomenological analysis indicates a significant relation  
565 between regional ABL-FT water vapor exchange and precipitation anomalies.

566 This work quantitatively reveals the climatological basic state of ABL-FT water vapor  
567 exchange flux over Eastern China and demonstrates its significance in regulating the  
568 atmospheric water cycle. The results may provide new insights for understanding and  
569 predicting precipitation anomalies on large scales.

#### 570 **Data availability**

571 The data in this study are available from the corresponding author ([xhcai@pku.edu.cn](mailto:xhcai@pku.edu.cn)).

#### 572 **Author contribution**

573 XHC and XPJ designed the research. LK and HSZ collected the data. XPJ performed the  
574 simulations and wrote the paper. XHC reviewed and commented on the paper. QQH, YS, XSW  
575 and TZ participated in the discussion of the article.

#### 576 **Competing interests**

577 The authors declare that they have no conflict of interest.

#### 578 **Acknowledgements**

579 This work was supported by National Key Research and Development Program of China  
580 (2018YFC0213204).

#### 581 **References**

- 582 Adebisi, A. A., P. Zuidema, and S. J. Abel, 2015: The Convolution of Dynamics and Moisture  
583 with the Presence of Shortwave Absorbing Aerosols over the Southeast Atlantic, *J. Climate*,  
584 28, 1997-2024, doi:10.1175/jcli-d-14-00352.1.
- 585 Allan, R. P., 2012: The Role of Water Vapour in Earth's Energy Flows, *Surv. Geophys.*, 33,  
586 557-564, doi: 10.1007/s10712-011-9157-8.
- 587 Andrey, J., E. Cuevas, M. C. Parrondo, S. Alonso-Perez, A. Redondas, and M. Gil-Ojeda, 2014:  
588 Quantification of ozone reductions within the Saharan air layer through a 13-year  
589 climatologic analysis of ozone profiles, *Atmos. Environ.*, 84, 28-34,  
590 doi:10.1016/j.atmosenv.2013.11.030.



- 591 Bailey, A., D. Toohey, and D. Noone, 2013: Characterizing moisture exchange between the  
592 Hawaiian convective boundary layer and free troposphere using stable isotopes in water, *J.*  
593 *Geophys. Res.-Atmos.*, 118, 8208-8221, doi:10.1002/jgrd.50639.
- 594 Boutle, I. A., R. J. Beare, S. E. Belcher, A. R. Brown, and R. S. Plant, 2010: The Moist  
595 Boundary Layer under a Mid-latitude Weather System, *Bound.-Layer Meteor.*, 134, 367-  
596 386, doi:10.1007/s10546-009-9452-9.
- 597 Chen, F., and J. Dudhia, 2001: Coupling an advanced land surface-hydrology model with the  
598 Penn State-NCAR MM5 modeling system. Part I: Model implementation and sensitivity.  
599 *Mon. Weather Rev.*, 129(4), 569-585, doi:10.1175/1520-  
600 0493(2001)129<0569:caalsh>2.0.co.
- 601 Dacre, H. F., S. L. Gray, and S. E. Belcher, 2007: A case study of boundary layer ventilation  
602 by convection and coastal processes. *J. Geophys. Res.-Atmos.*, 112(D17),  
603 doi:10.1029/2006jd007984.
- 604 Dahinden, F., and Coauthors, 2021: Disentangling different moisture transport pathways over  
605 the eastern subtropical North Atlantic using multi-platform isotope observations and high-  
606 resolution numerical modelling, *Atmos. Chem. Phys.*, 21, 16319-16347, doi:10.5194/acp-  
607 21-16319-2021.
- 608 Diaz, H. F., 2000: *El Niño and the Southern Oscillation: Multiscale Variability and Global and*  
609 *Regional Impacts*, Cambridge University Press: Cambridge, UK.
- 610 Domroes, M. and Peng, G., 1988: *The Climate of China*, Springer, Berlin.
- 611 Dudhia, J., 1989: Numerical study of convection observed during the winter monsoon  
612 experiment using a mesoscale two-dimensional model. *J. Atmos. Sci.*, 46(20), 3077-3107,  
613 doi:10.1175/1520-0469(1989)046<3077:nsocod>2.0.co;2.
- 614 Felix Correia Filho, W. L., J. F. de Oliveira-Junior, C. A. da Silva Junior, and D. d. B. Santiago,  
615 2021: Influence of the El Niño-Southern Oscillation and the synoptic systems on the rainfall  
616 variability over the Brazilian Cerrado via Climate Hazard Group InfraRed Precipitation  
617 with Station data, *Int. J. Climatol.*, doi:10.1002/joc.7417.
- 618 Fritz, C., and Z. Wang, 2013: A Numerical Study of the Impacts of Dry Air on Tropical  
619 Cyclone Formation: A Development Case and a Nondevelopment Case, *J. Atmos. Sci.*, 70,  
620 91-111, doi:10.1175/jas-d-12-018.1.
- 621 Ghannam, K., Duman, T., Salesky, S. T., Chamecki, M., and Katul, G., 2017: The non-local  
622 character of turbulence asymmetry in the convective atmospheric boundary layer, 143, 494-  
623 507, doi: 10.1002/qj.2937.
- 624 Gonzalez, A., F. J. Exposito, J. C. Perez, J. P. Diaz, and D. Taima, 2013: Verification of  
625 precipitable water vapor in high-resolution WRF simulations over a mountainous  
626 archipelago, *Q. J. Roy. Meteor. Soc.*, 139, 2119-2133, doi: 10.1002/qj.2092.
- 627 Gonzalez, Y., Schneider, M., Dyroff, C., Rodriguez, S., Christner, E., Garcia, O. E., Cuevas,  
628 E., Bustos, J. J., Ramos, R., Guirado-Fuentes, C., Barthlott, S., Wiegele, A., and Sepulveda,  
629 E., 2016: Detecting moisture transport pathways to the subtropical North Atlantic free



- 630 troposphere using paired H<sub>2</sub>O- $\delta$  D in situ measurements, *Atmos. Chem. Phys.*, 16,  
631 4251-4269, doi:10.5194/acp-16-4251-2016.
- 632 Grell, G. A., and D. Devenyi, 2002: A generalized approach to parameterizing convection  
633 combining ensemble and data assimilation techniques, *Geophys. Res. Lett.*, 29,  
634 doi:10.1029/2002gl015311.
- 635 Gvozdkova, B. and M. Muller, 2021: Moisture fluxes conducive to central European extreme  
636 precipitation events, *Atmos. Res.*, 248, doi:10.1016/j.atmosres.2020.105182.
- 637 Hagos, S. M. and K. H. Cook, 2007: Dynamics of the West African monsoon jump, *J. Climate*,  
638 20, 5264-5284, doi:10.1175/2007jcli1533.1.
- 639 Harries, J., and Coauthors, 2008: The far-infrared Earth, *Rev. Geophys.*, 46,  
640 doi:10.1029/2007rg000233.
- 641 Henne, S., M. Furger, and A. S. H. Prevot, 2005: Climatology of mountain venting-induced  
642 elevated moisture layers in the lee of the Alps, *J. Appl. Meteorol.*, 44, 620-633,  
643 doi:10.1175/jam2217.1.
- 644 Hirota, N., T. Ogura, H. Tatebe, H. Shiogama, M. Kimoto, and M. Watanabe, 2018: Roles of  
645 Shallow Convective Moistening in the Eastward Propagation of the MJO in MIROC6, *J.*  
646 *Climate*, 31, 3033-3047, doi:10.1175/jcli-d-17-0246.1.
- 647 Hong, S. Y., Y. Noh, and J. Dudhia, 2006: A new vertical diffusion package with an explicit  
648 treatment of entrainment processes. *Mon. Weather Rev.*, 134(9), 2318-2341,  
649 doi:10.1175/mwr3199.1.
- 650 Hong, S. Y., and J. J. Lim, 2006: The WRF single-moment 6-class microphysics scheme  
651 (WSM6). *J. Korean Meteorol. Soc.*, 42, 129-151.
- 652 Hov, Ø., and Flatøy, F., 1997: Convective redistribution of ozone and oxides of nitrogen in the  
653 troposphere over Europe in summer and fall. *Journal of Atmospheric Chemistry*, 28(1-3),  
654 319-337, <https://doi.org/10.1023/a:1005780730600>.
- 655 Jain, S., and S. C. Kar, 2017: Transport of water vapor over the Tibetan Plateau as inferred  
656 from the model simulations, *J. Atmos. Solar-Terr. Phys.*, 161, 64-75,  
657 doi:10.1016/j.jastp.2017.06.016.
- 658 Jin, X. P., X. H. Cai, Q. Q. Huang, X. S. Wang, Y. Song, and T. Zhu, 2021: Atmospheric  
659 Boundary Layer-Free Troposphere Air Exchange in the North China Plain and its Impact  
660 on PM<sub>2.5</sub> Pollution, *J. Geophys. Res.-Atmos.*, 126, doi:10.1029/2021jd034641.
- 661 Jin, X. P., X. H. Cai, M. Y. Yu, Y. Song, X. S. Wang, L. Kang, and H. S. Zhang, 2020:  
662 Diagnostic analysis of wintertime PM<sub>2.5</sub> pollution in the North China Plain: The impacts  
663 of regional transport and atmospheric boundary layer variation. *Atmos. Environ.*, 224,  
664 117346, doi: 10.1016/j.atmosenv.2020.117346.
- 665 Kain, J. S., 2004: The Kain-Fritsch convective parameterization: An update. *J. Appl. Meteorol.*,  
666 43(1), 170-181, doi:10.1175/1520-0450(2004)043<0170:tkcpau>2.0.co;2.
- 667 Kiehl, J. T., and K. E. Trenberth, 1997: Earth's annual global mean energy budget, *Bull. Am.*  
668 *Meteorol. Soc.*, 78, 197-208, doi:10.1175/1520-0477(1997)078<0197:eagmeb>2.0.co;2.



- 669 Knippertz, P., and H. Wernli, 2010: A Lagrangian Climatology of Tropical Moisture Exports  
670 to the Northern Hemispheric Extratropics, *J. Climate*, 23, 987-1003,  
671 doi:10.1175/2009jcli3333.1.
- 672 Kossmann, M., U. Corsmeier, S. F. J. de Wekker, F. Fiedler, R. Vogtlin, N. Kalthoff, H. Gusten,  
673 and B. Neininger, 1999: Observations of handover processes between the atmospheric  
674 boundary layer and the free troposphere over mountainous terrain. *Contrib. Atmos. Phys.*,  
675 72(4), 329-350.
- 676 Kousky, V. E., M. T. Kagano, and I. F. A. Cavalcanti, 1984: A review of the southern  
677 oscillation-oceanic-atmospheric circulation changes and related rainfall anomalies, *Tellus*.  
678 A., 36, 490-504, doi: 10.1111/j.1600-0870.1984.tb00264.x.
- 679 Li, Q. H., B. G. Wu, J. L. Liu, H. S. Zhang, X. H. Cai, and Y. Song, 2020: Characteristics of  
680 the atmospheric boundary layer and its relation with PM<sub>2.5</sub> during haze episodes in winter  
681 in the North China Plain. *Atmos. Environ.*, 223, 117265,  
682 doi:org/10.1016/j.atmosenv.2020.117265.
- 683 Lin, Y. L., R. D. Farley, and H. D. Orville, 1983: Bulk parameterization of the snow field in a  
684 cloud model. *J. Climate Appl. Meteorol.*, 22(6), 1065-1092, doi:10.1175/1520-  
685 0450(1983)022<1065:bpotsf>2.0.co;2.
- 686 Liu, B. J., Tan, X. Z., Gan, T. Y., Chen, X. H., Lin, K. R., Lu, M. Q., et al. (2020), Global  
687 atmospheric moisture transport associated with precipitation extremes: Mechanisms and  
688 climate change impacts, *Wires. Water*, 7, doi:10.1002/wat2.1412.
- 689 Liu, S. Y., and X. Z. Liang, 2010: Observed Diurnal Cycle Climatology of Planetary Boundary  
690 Layer Height. *J. Climate*, 23, 5790-5809, doi:10.1175/2010jcli3552.1.
- 691 Marchukova, O. V., E. N. Voskresenskaya, and A. S. Lubkov, 2020: Diagnostics of the La  
692 Niña events in 1900–2018, *Earth Environ. Sci.*, 606, 012036, doi:10.1088/1755-  
693 1315/606/1/012036.
- 694 McKendry, I. G., and J. Lundgren, 2000: Tropospheric layering of ozone in regions of  
695 urbanized complex and/or coastal terrain: a review, *Prog. Phys. Geog.*, 24(3), 329–354, doi:  
696 10.1177/030913330002400302.
- 697 Minschwaner, K., and A. E. Dessler, 2004: Water vapor feedback in the tropical upper  
698 troposphere: model results and observations. *J. Climate*, 17, 1272–1282, doi:  
699 10.1175/1520-0442(2004)017<1272:WVFITT>2.0.CO;2.
- 700 Miura, H., M. Satoh, H. Tomita, A. T. Noda, T. Nasuno, and S. Iga, 2007: A short-duration  
701 global cloud-resolving simulation with a realistic land and sea distribution, *Geophys. Res.*  
702 *Letts.*, 34, doi:10.1029/2006gl027448.
- 703 Mlawer, E. J., S. J. Taubman, P. D. Brown, M. J. Iacono, and S. A. Clough, 1997: Radiative  
704 transfer for inhomogeneous atmospheres: RRTM, a validated correlated-k model for the  
705 longwave. *J. Geophys. Res.-Atmos.*, 102(D14), 16663-16682, doi:10.1029/97jd00237.
- 706 Newell, R. E., Y. Zhu, and C. Scott, 1992: Tropospheric rivers-a pilot-study, *Geophys. Res.*  
707 *Letts.*, 19, 2401-2404, doi:10.1029/92gl02916.



- 708 Perez, J. C., B. Garcia-Lorenzo, J. P. Diaz, A. Gonzalez, F. Exposito, and M. Insausti, 2010:  
709 Forecasting precipitable water vapor at the Roque de los Muchachos Observatory,  
710 Conference on Ground-Based and Airborne Telescopes III, San Diego, CA, 2010 Jun 27-  
711 Jul 02, WOS:000285506700149, doi:10.1117/12.859453.
- 712 Pilinis, C., J. H. Seinfeld, and D. Grosjean, 1989: Water-content of atmospheric aerosols,  
713 Atmos. Environ., 23, 1601-1606, doi:10.1016/0004-6981(89)90419-8.
- 714 Qian, X., Y. Yao, H. Wang, L. Zou, Y. Li, and J. Yin, 2020: Validation of the WRF Model for  
715 Estimating Precipitable Water Vapor at the Ali Observatory on the Tibetan Plateau, Publ.  
716 Astron. Soc. Pac., 132, doi:10.1088/1538-3873/abc22d.
- 717 Sherwood, S. C., 1996: Maintenance of the free-tropospheric tropical water vapor  
718 distribution .1. Clear regime budget, J. Climate, 9, 2903-2918, doi:10.1175/1520-  
719 0442(1996)009<2903:motfft>2.0.co;2.
- 720 Sherwood, S. C., R. Roca, T. M. Weckwerth, and N. G. Andronova., 2010: Tropospheric water  
721 vapor, convection, and climate. Rev. Geophys., 48, RG2001, doi: 10.1029/2009RG000301.
- 722 Sinclair, V. A., S. E. Belcher, and S. L. Gray, 2010: Synoptic Controls on Boundary-Layer  
723 Characteristics, Bound-Layer Meteor., 134(3), 387-409, doi:10.1007/s10546-009-9455-6.
- 724 Sodemann, H., and A. Stohl, 2013: Moisture Origin and Meridional Transport in Atmospheric  
725 Rivers and Their Association with Multiple Cyclones, Mon. Weather Rev., 141, 2850-2868,  
726 doi:10.1175/mwr-d-12-00256.1.
- 727 Stull, R. B., 1988: An Introduction to Boundary Layer Meteorology. Kluwer Acad., Dordrecht,  
728 Netherlands, doi:10.1007/978-94-009-3027-8.
- 729 Sun, L., B. Z. Shen, and B. Sui, 2010: A Study on Water Vapor Transport and Budget of Heavy  
730 Rain in Northeast China, Adv. Atmos. Sci., 27, 1399-1414, doi:10.1007/s00376-010-9087-  
731 2.
- 732 Tabazadeh, A., M. L. Santee, M. Y. Danilin, H. C. Pumphrey, P. A. Newman, P. J. Hamill, and  
733 J. L. Mergenthaler, 2000: Quantifying denitrification and its effect on ozone recovery,  
734 Science, 288, 1407-1411, doi:10.1126/science.288.5470.1407.
- 735 van Dop, H. and Verver, G., 2001: Countergradient transport revisited, J. Atmos. Sci., 58,  
736 2240-2247, doi: 10.1175/1520-0469(2001)058<2240:CTR>2.0.CO;2.
- 737 Walker, G. T., and E. W. Bliss, 1932: World weather V., Mem. Roy. Meteor. Soc., 4, 53-84.
- 738 Walker, G. T., and E. W. Bliss, 1937: World weather VI., Mem. Roy. Meteor. Soc., 4, 119-  
739 139.
- 740 Wang, L. J., C. Cai, and H. Y. Zhang, 2020: Circulation characteristics and critical systems of  
741 summer precipitation in eastern China under the background of two types of ENSO events,  
742 Trans. Atmos. Sci., 43(4), 617-629, doi:10.13878/j.cnki.dqkxxb.20180817002.
- 743 Weigel, A. P., F. K. Chow, and M. W. Rotach, 2007: The effect of mountainous topography  
744 on moisture exchange between the "surface" and the free atmosphere, Bound-Layer  
745 Meteor., 125, 227-244, doi:10.1007/s10546-006-9120-2.



- 746 Wolter, K., and M. S. Timlin, 2011: El Niño/Southern Oscillation behaviour since 1871 as  
747 diagnosed in an extended multivariate ENSO index (MEI.ext), *Int. J. Climatol.*, 31, 1074-  
748 1087, doi:10.1002/joc.2336.
- 749 Wong, S., C. M. Naud, B. H. Kahn, L. T. Wu, and E. J. Fetzer, 2018: Coupling of Precipitation  
750 and Cloud Structures in Oceanic Extratropical Cyclones to Large-Scale Moisture Flux  
751 Convergence, *J. Climate*, 31, 9565-9584, doi:10.1175/jcli-d-18-0115.1.
- 752 Wu, J. R., and Coauthors, 2019: Is water vapor a key player of the wintertime haze in North  
753 China Plain?, *Atmos. Chem. Phys.*, 19, 8721-8739, doi:10.5194/acp-19-8721-2019.
- 754 Wypych, A., B. Bochenek, and M. Rozycki, 2018: Atmospheric Moisture Content over Europe  
755 and the Northern Atlantic, *Atmosphere*, 9, doi:10.3390/atmos9010018.
- 756 You, T., R. G. Wu, G. Liu, and Z. Y. Chai, 2021: Contribution of precipitation events with  
757 different consecutive days to rainfall change over Asia during ENSO years, *Theor. Appl.*  
758 *Climatol.*, 144, 147–161, doi: 10.1007/s00704-021-03538-8.
- 759 Zhang, H. G., Hu, Y. T., Cai, J. D., Li, X. J., Tian, B. H., Zhang, Q. D. and An, W., 2020:  
760 Calculation of evapotranspiration in different climatic zones combining the long-term  
761 monitoring data with bootstrap method, *Environmental Research*, 191,  
762 doi:10.1016/j.envres.2020.110200.
- 763 Zheng, J., J. Bian, Q. Ge, Z. Hao, Y. Yin, and Y. Liao, 2013: The climate regionalization in  
764 China for 1981-2010, *Chinese Science Bulletin*, 58, 3088-3099, doi: 10.1360/972012-1491.
- 765 Zhou, T. J., and R. C. Yu, 2005: Atmospheric water vapor transport associated with typical  
766 anomalous summer rainfall patterns in China, *J. Geophys. Res.-Atmos.*, 110,  
767 doi:10.1029/2004jd005413.
- 768 Zhu, Y., and R. E. Newell, 1998: A proposed algorithm for moisture fluxes from atmospheric  
769 rivers, *Mon. Weather. Rev.*, 126, 725-735, doi:10.1175/1520-  
770 0493(1998)126<0725:apafmf>2.0.co;2.